

An atomic Fabry-Perot interferometer using a pulsed interacting Bose-Einstein condensate

P. Manju^{1,*}, K. S. Hardman¹, P. B. Wigley¹, J. D. Close¹, N. P. Robins¹, and S. S. Szigeti¹

¹Atomlaser and Quantum Sensors Group, Department of Quantum Science, Research School of Physics, The Australian National University, Canberra 2601, Australia

*manju.perumbil@anu.edu.au

ABSTRACT

We numerically demonstrate atomic Fabry-Perot resonances for a pulsed interacting Bose-Einstein condensate (BEC) source transmitting through double Gaussian barriers. These resonances are observable for an experimentally-feasible parameter choice, which we determined using a previously-developed analytical model for a plane matter-wave incident on a double rectangular barrier system. By simulating an effective one-dimensional Gross-Pitaevskii equation, we investigate the effect of atom number, scattering length, and BEC momentum width on the resonant transmission peaks. For ⁸⁵Rb atomic sources with the current experimentally-achievable momentum width of $0.02\hbar k_0$ [$k_0 = 2\pi/(780 \text{ nm})$], we show that reasonably high contrast Fabry-Perot resonant transmission peaks can be observed using a) non-interacting BECs of 10^5 atoms, b) interacting BECs of 10^5 atoms with s -wave scattering lengths $a_s = \pm 0.1a_0$ [a_0 is the Bohr radius], and c) interacting BECs of 10^3 atoms with $a_s = \pm 1.0a_0$. Our theoretical investigation impacts any future experimental realisation of an atomic Fabry-Perot interferometer with an ultracold atomic source.

Introduction

Understanding the different and complementary properties of atoms compared with photons has advanced both fundamental and applied physics. In direct analogy to optical systems, atomic matter waves can be coherently focussed¹, reflected², diffracted³ and interfered⁴. These basic atom-optical elements have been combined to construct more sophisticated analogue systems such as atomic waveguides⁵, atom lasers^{6,7} and atom interferometers^{8,9}. Atomic properties such as mass, tunable dispersion, and differing degrees of freedom make these analogue systems versatile measurement tools. Atom interferometers, for example, have enabled state-of-the-art measurements of the fine structure constant^{10,11} and inertial fields such as gravity¹²⁻¹⁴ and rotations^{15,16}.

In this paper, we consider the atomic analogue of a Fabry-Perot interferometer. Optical Fabry-Perot interferometry is used for many fundamental scientific and industrial applications, including linewidth measurements of continuous wave and pulsed lasers¹⁷, laser phase and frequency stabilisation¹⁸ and precision sensing^{19,20}. An atomic Fabry-Perot interferometer could offer new sensing capabilities by exploiting the atomic mass and tunable dispersion. Furthermore, the analogous mirrors, formed using optical potentials, allow for real-time and versatile control of the system. Previous theoretical work has investigated the resonance properties of Fabry-Perot interferometers using matterwaves²¹, their use in velocity selection^{22,23} and the identification of bosonic and fermionic isotopes of an element^{24,25}. In order to fully exploit the benefits of this atomic analogue, the transmission characteristics of an atomic Fabry-Perot interferometer in an experimentally realisable regime must be understood.

Much like the optical Fabry-Perot interferometer, the atomic analogue requires a narrow linewidth source to fully exploit the interference effects of the system. The properties of an optical laser make it a superior source for a Fabry-Perot interferometer compared with a broadband light source. Bose-Einstein condensates (BECs) display many properties analogous to a laser, including high coherence and narrow momentum width, which have proven advantageous for precision atom interferometry²⁶⁻²⁸. Although many theoretical proposals have shown that atomic Fabry-Perot interferometers can be developed using continuous wave (CW) atom laser beams constructed from interacting and non-interacting BEC sources^{23,29-33}, a true CW atom laser has yet to be experimentally realised³⁴. In contrast, a pulsed atom laser, formed by releasing and propagating a BEC, is readily achievable in atom laboratories.

This paper investigates the properties of an atomic Fabry-Perot interferometer in an experimentally realisable parameter regime^{35,36}. We use a simple analytic model³⁷ for rectangular potentials to study the dependence of cavity finesse and transmission coefficient on barrier width, barrier height, cavity length, initial momentum of the atoms, and the momentum width of the atomic cloud. This allows us to identify a parameter regime where high contrast, narrow peaks are observable in the transmission spectrum. Using these established parameters, we numerically simulate the propagation of a pulsed ⁸⁵Rb BEC

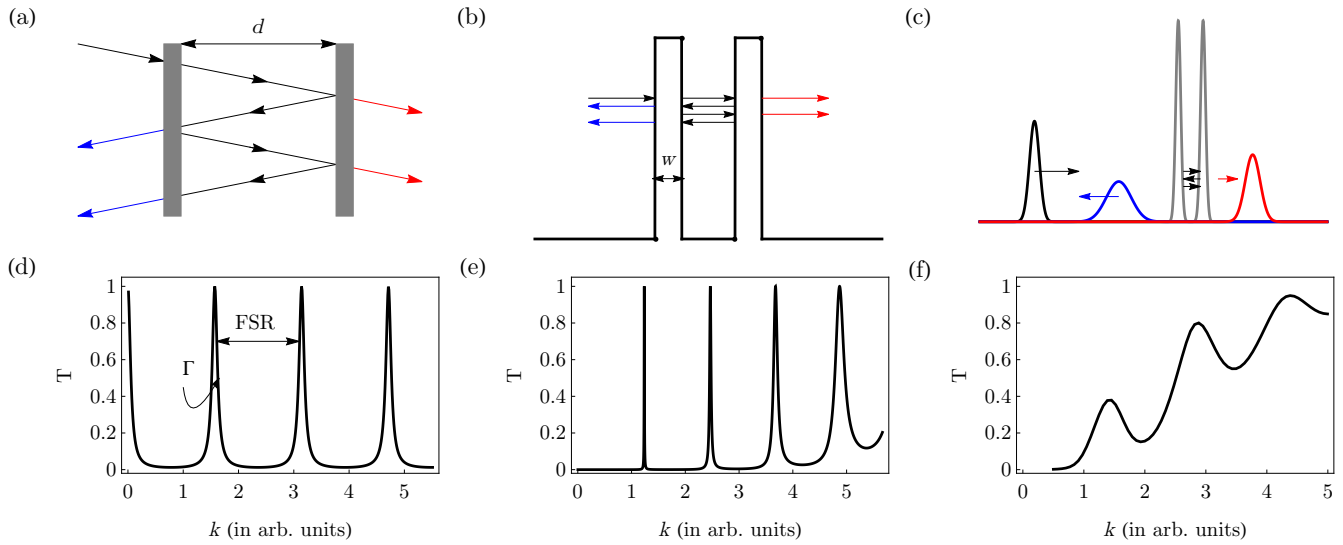


Figure 1. Schematic diagrams of Fabry-Perot interferometers and their respective transmission spectra. The top row depicts the transmission and reflection of (a) narrow band light through an optical Fabry-Perot interferometer, (b) a narrow band matterwave through a rectangular double barrier, and (c) a broad band Gaussian wavepacket (i.e. a non-interacting BEC with finite momentum width) through double Gaussian barriers. Outside the cavity, the black arrow represents the incident wave, whilst blue and red denote the reflected and transmitted parts of the wave, respectively. (d), (e) and (f) show corresponding transmission resonance peaks. Here d is the cavity length, w is the barrier width, T is the transmission coefficient, FSR is the free spectral range of the resonance spectrum, and Γ is the cavity linewidth.

through a cavity formed via double Gaussian barriers. ^{85}Rb is ideal for this study due to its inter-atomic interactions that are tunable via a Feshbach resonance^{38,39}. We investigate the resonant transmission process for an interacting and non-interacting BEC and study the effect of the condensate's momentum width and inter-atomic interactions on resonant transport through the double barrier system. Using the experimentally feasible parameters we have determined, we demonstrate resonant transmission, requiring a momentum width achievable using delta-kick cooling^{36,40,41}. We show that the transmission coefficient and finesse can be improved by reducing the initial cloud's momentum width, allowing for resonant transmission even in the interacting case.

Fabry-Perot Interferometry

In order to build an understanding of the parameter dependencies, we initially consider an idealised optical Fabry-Perot cavity, extending this to an analytic model describing the atomic analogue. Using this analytic model in tandem with known experimental limitations, we determine a feasible parameter regime for realising an atomic Fabry Perot interferometer. These parameters are then used to simulate the more complex model involving barriers described by Gaussian potentials and a finite momentum width BEC, including inter-atomic interactions. This progression is illustrated in Fig. 1.

An ideal optical Fabry-Perot interferometer is made of two parallel mirrors separated by a distance, d (cavity length), as shown in Fig. 1(a). The light entering the cavity undergoes multiple reflections from the mirrors and interferes with itself. Constructive interference enhances the light inside the cavity, leading to resonant transmission out of the cavity. Here we consider the ideal case where the mirror reflectivity is independent of the wavelength of light. Resonant transmission peaks, illustrated in Fig. 1(d), are obtained by scanning the wave number (k) of the incident light. These peaks have a linewidth⁴²

$$\Gamma = \frac{c}{2\pi d} \frac{1 - \sqrt{R_1 R_2}}{(R_1 R_2)^{1/4}}, \quad (1)$$

and are separated by the free spectral range

$$\text{FSR} = \frac{c}{2d}, \quad (2)$$

where R_1 and R_2 describe the reflectivity of each mirror forming the cavity, and c is the velocity of light in vacuum. These

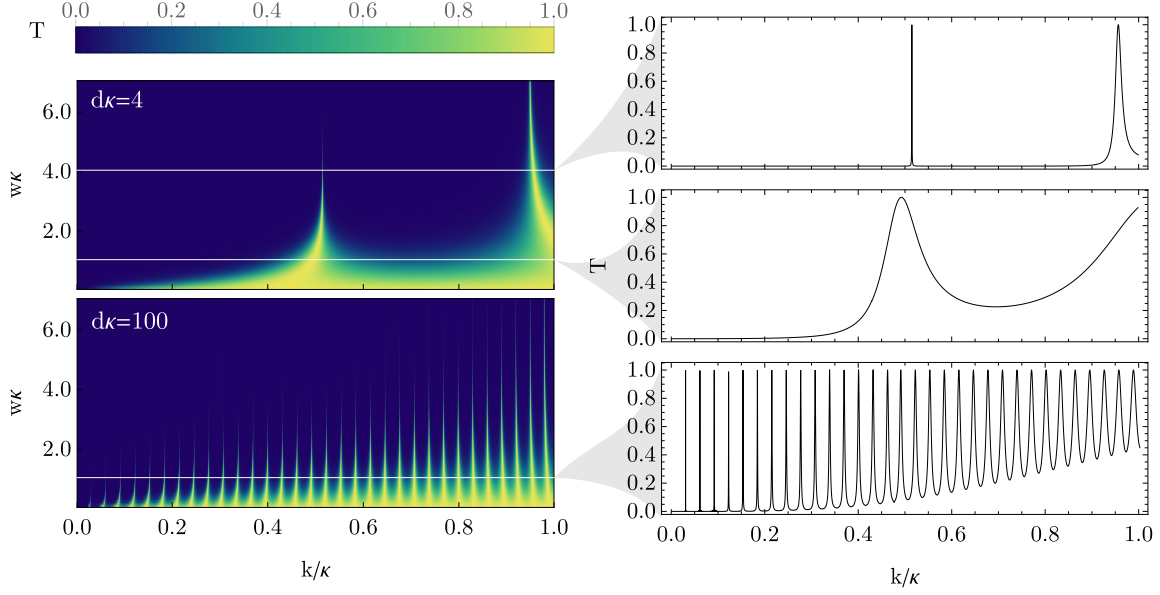


Figure 2. Transmission coefficient of a narrow-band beam of particles passing through a double rectangular barrier system [Eq. (4) - see also Fig. 1(b) and (d)] for (top left) $d\kappa = 4$ and (bottom left) $d\kappa = 100$. The three plots on the right-hand side show cross sections from the left plot at (top) $w\kappa = 4, d\kappa = 4$, (middle) $w\kappa = 1, d\kappa = 4$, and (bottom) $w\kappa = 1, d\kappa = 100$. For a fixed barrier height (fixed κ), the cavity linewidth decreases with increasing barrier width and/or cavity length, whereas the FSR decreases with increasing cavity length. Here w, d, k and κ are the barrier width, cavity length, and wave vectors of the particles and barriers, respectively.

quantities, along with the finesse

$$\mathcal{F} = \frac{\text{FSR}}{\Gamma} = \frac{\pi(R_1 R_2)^{1/4}}{1 - \sqrt{R_1 R_2}}, \quad (3)$$

are the figures of merit for an optical Fabry-Perot interferometer⁴².

In an atomic Fabry-Perot interferometer, the incoming light is replaced by atoms and the mirrors are replaced by laser-induced potential barriers. The atomic system provides key differences including atomic mass, inter-atomic interactions, and mirrors where the key parameters can be tuned. This results in changes to the transmission characteristics of the atomic system compared with that of the optical system. This is qualitatively illustrated by Fig. 1(e) and (f). In contrast to the ideal optical Fabry-Perot interferometer, the atomic system displays changes in the FSR and Γ as the wave number of the incoming particles changes. To analyse the characteristics of a matter wave Fabry-Perot interferometer, we use a previously developed analytical model³⁷. This model assumes a plane wave of non-interacting particles, with energy E , transmitting through two symmetric rectangular barriers of width w , height V_0 , and separation distance d [see Fig. 1(b)].

The transmission coefficient, T can be described using the dimensionless parameters $w\kappa$, k/κ and $d\kappa$, where $k = \sqrt{2mE}/\hbar$ and $\kappa = \sqrt{2mV_0}/\hbar$ are the wave vectors of particles and barriers, respectively. Specifically,

$$T = \frac{1}{1 + \frac{4}{\pi^2} [\mathcal{F}(w\kappa, k/\kappa)]^2 \sin^2[d\kappa \times k/\kappa + \phi(w\kappa, k/\kappa)]}, \quad (4)$$

where

$$\mathcal{F}(w\kappa, k/\kappa) = \frac{\pi\sqrt{R(w\kappa, k/\kappa)}}{1 - \sqrt{R(w\kappa, k/\kappa)}}, \quad (5)$$

$$R(w\kappa, k/\kappa) = \frac{[M_+(k/\kappa)]^2}{[M_-(k/\kappa)]^2 + \coth^2(w\kappa\sqrt{1 - (k/\kappa)^2})}, \quad (6)$$

$$M_{\pm}(k/\kappa) = \frac{1}{2} \left(\frac{\sqrt{1 - (k/\kappa)^2}}{(k/\kappa)} \pm \frac{(k/\kappa)}{\sqrt{1 - (k/\kappa)^2}} \right), \quad (7)$$

$$\phi(w\kappa, k/\kappa) = \frac{\pi}{2} - \tan^{-1} \left[M_-(k/\kappa) \tanh \left(w\kappa\sqrt{1 - (k/\kappa)^2} \right) \right]. \quad (8)$$

Here \mathcal{F} and R are interpreted as the cavity's finesse and mirror (rectangular barrier) reflectivity. The relationship of the transmission coefficient to $w\kappa$ and k/κ is illustrated for two different values of $d\kappa$ in Fig. 2. The three plots on the right-hand side show cross sections from the left plot for $d\kappa = 4$ with $w\kappa = 4$ (top) and $w\kappa = 1$ (middle) in addition to $d\kappa = 100$ with $w\kappa = 1$ (bottom). The first two cross sections show that the cavity linewidth decreases with increasing barrier width, for a fixed barrier height and cavity length. The second and third cross sections show that both FSR and linewidth decrease with increasing cavity length, for a fixed barrier height and width. In contrast to the ideal optical Fabry-Perot interferometer, the linewidth increases with increasing k for fixed barrier height and barrier width. This behaviour is due to the strong wavelength-dependence of the mirror reflectivity in the atomic Fabry-Perot interferometer. Similar effects would be seen when considering an optical cavity with strong wavelength dependent reflectivities.

Now we consider the finesse of the cavity, which is given by Eq. (5). The finesse only depends upon the dimensionless parameters $w\kappa$ and k/κ .

As shown in Fig. 3, the finesse decreases with increasing k/κ and increases with increasing $w\kappa$. Therefore, for a fixed barrier height, an increase in particle momentum causes a decrease in finesse, whereas an increase in barrier width causes an increase in finesse. Again, this behaviour is different to the ideal optical Fabry-Perot interferometer, and is due to the mirror reflectivity's dependence on barrier height, barrier width, and the energy of the incoming atoms.

The above analysis reveals the parameter regimes needed to make an atomic Fabry-Perot interferometer with desirable qualities such as high finesse and narrow linewidth. However, we do not have complete freedom in our parameter choice, as the limitations of current cold-atom technology impose additional constraints. We discuss these additional constraints below, and combine them with the results of the above analytic model to determine an experimentally-feasible parameter regime for realising an atomic Fabry-Perot interferometer. The operation of an atomic Fabry-Perot interferometer depends sensitively on the following parameters:

- **Momentum width of the atomic cloud.** The above analytical study assumes a plane matter wave with infinitely narrow momentum width. In reality, all atomic clouds have finite momentum widths. In order to observe Fabry-Perot resonances, ideally the momentum spread of the atomic source needs to be much less than the FSR and linewidth of the cavity. To date, the smallest experimentally-achieved momentum width for an atomic cloud is $0.02\hbar k_0$ ³⁶, which was obtained by delta-kick cooling a rubidium BEC (here $k_0 = 8.06 \times 10^6 \text{m}^{-1}$ is the wave vector of the light used to impart momentum through Bragg spectroscopy on the ⁸⁵Rb D_2 transition⁴³⁻⁴⁵). Hence, we aim to select parameters that give a cavity linewidth and FSR larger than this value.
- **Barrier width.** Although narrow resonances and a high finesse are desirable, the lower bound on experimentally-achievable BEC momentum width requires us to operate in a regime where the cavity linewidth is relatively broad. We find that selecting $w\kappa = 1$ is a good compromise, since it gives resonance peaks that are wide enough to be observable yet still narrow enough to be potentially useful. Additionally, the minimum achievable barrier width is restricted by the diffraction limit of the laser, which for our system is on the order of $1 \mu\text{m}$. We fix the barrier width to this minimum, i.e. $w = 1 \mu\text{m}$; a significantly larger choice for w would require a smaller κ , resulting in a cavity spectrum that could only be observed by scanning unachievably small values of k .
- **Barrier height.** Fixing w and $w\kappa$ completely determines the barrier height. Explicitly, $\kappa = 1\mu\text{m}^{-1} = 0.12414k_0$, corresponding to a barrier height of $V_0 = \hbar^2\kappa^2/(2m) = 3.83 \times 10^{-32} \text{J}$.
- **Cavity length.** The finesse of the cavity does not depend on the cavity length. However, in order to reduce the overlap between the two laser-induced barriers experimentally, we need a cavity length that is larger than the barrier width. Additionally, momentum width consideration require a regime where the cavity linewidth is relatively broad (see above).

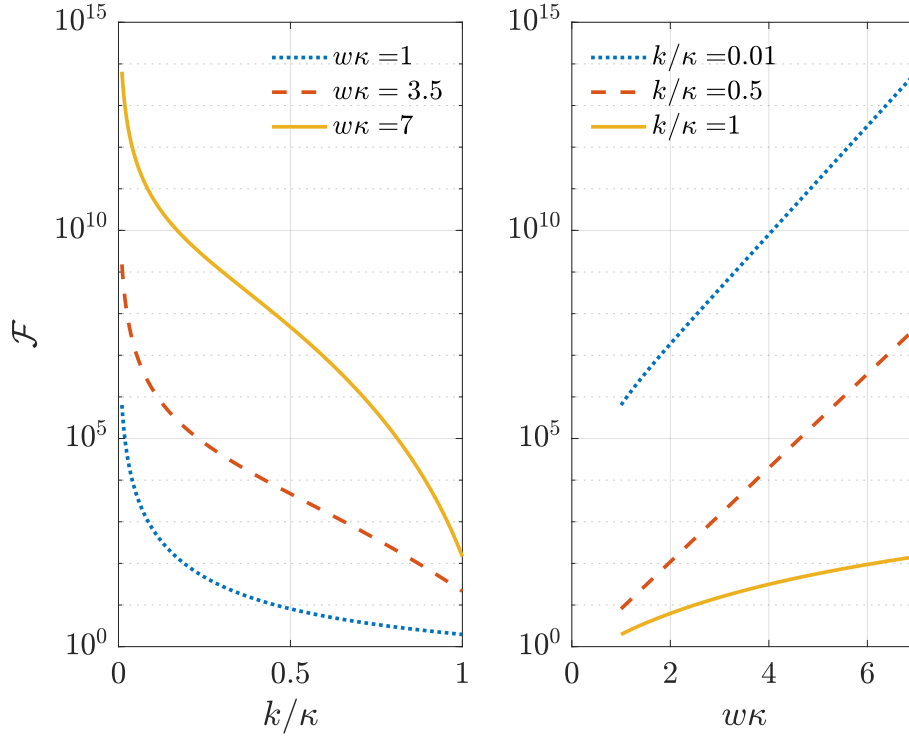


Figure 3. For a beam of particles transmitting through a double rectangular barrier system, finesse is plotted as a function of dimensionless particle wave vector (k/κ) and barrier width $w\kappa$, where κ is the wave vector corresponding to the barrier in units of m^{-1} . For a fixed barrier height, finesse decreases with increasing momentum of the particle, but increases with increasing barrier width.

Figure 2 shows that as $d\kappa$ decreases, both FSR and linewidth increase. Therefore, in order to observe at least two broad linewidth transmission peaks, we choose $d\kappa = 4$. This gives a cavity length of $d = 4\mu\text{m}$, which is larger than the chosen barrier width ($d = 4w$).

- **Momentum imparted to the atoms.** Finally, in order to observe resonance peaks, we must be able to scan the incident energy of the atoms. This can be done by imparting momentum to the atoms through, for example, Bragg transitions^{13,44}. For the above parameter choices, at least two peaks are observable by scanning k/κ from 0.01 to 1.2 (see Fig. 2). This corresponds to k range of $k = 0.001k_0$ to $k = 0.1489k_0$.

Based on the above experimentally-feasible parameter choice, our simple analytic model predicts that resonant peaks should be observable with $\text{FSR} = 0.0687\hbar k_0$ (which is greater than the cloud momentum width, $0.02\hbar k_0$) and linewidth $\Gamma = 0.0097\hbar k_0$. This linewidth is about a factor of two smaller than the momentum width of the cloud, which is not ideal. Nevertheless, as we show below with more detailed theoretical modelling, Fabry-Perot resonances are observable in this regime. Indeed, the experimental system includes much more complexity than the simple analytical model considered above. For example, the barriers are created experimentally using blue-detuned lasers, which are more accurately modelled as Gaussian barriers, in contrast to the rectangular barriers used in the analytical model. Furthermore, BECs are finite momentum width sources that typically have non-negligible inter-atomic interactions. These inter-atomic interactions couple different momentum components of the cloud and also have a non-trivial effect on the transmission dynamics^{46–49}. Therefore, although the analytic study can guide our parameter choice, it cannot provide detailed modelling of an interacting BEC's transmission dynamics through double Gaussian barriers. This demands a numerical investigation.

Theoretical model for numerical simulation

The mean-field dynamics of a weakly-interacting BEC in a quasi-1D geometry are well-described by an effective 1D Gross-Pitaevskii equation (GPE)³⁰. In the case of an atomic Fabry-Perot interferometer, the three-body recombination loss rate can become significant due to the high density formed by the multiple reflections of the atoms between barriers. An effective 1D

GPE that phenomenologically includes a three-body recombination loss term is given by⁵⁰,

$$i\hbar \frac{\partial \psi(z,t)}{\partial t} = \left[-\frac{\hbar^2}{2m} \frac{\partial^2}{\partial z^2} + V(z) + g_{1D} |\psi(z,t)|^2 - i\hbar K_{1D} |\psi(z,t)|^4 \right] \psi(z,t), \quad (9)$$

where $\psi(z,t)$ is the macroscopic condensate wave function normalized to the total particle number, $N(t) = \int dz |\psi(z,t)|^2$, $V(z)$ is the external potential (a double Gaussian barrier potential during evolution), m is the atomic mass, and g_{1D} and K_{1D} are the effective 1D two-body interaction strength and three-body recombination loss rate coefficient, respectively.

Our effective 1D model assumes that the condensate's radial degrees of freedom are fixed during evolution, which is an acceptable approximation for propagation through a waveguide potential with tight radial confinement^{51,52}. If the atoms are initially condensed into a cylindrically-symmetric harmonic trap, then the radius of the BEC's radial distribution, R_{\perp} , is fixed to that of the ground state. Within the Thomas-Fermi regime, this is $R_{\perp} = \sqrt{2\mu_{3D}/(m\omega_{\perp}^2)}$, where $\mu_{3D} = [(15Ng_{3D}\omega_{\perp}^2 \omega_z(m/2)^{3/2})/(8\pi)]^{2/5}$ is the ground state chemical potential, ω_{\perp} and ω_z are the radial and axial trapping frequencies, respectively, N is the number of atoms, and $g_{3D} = 4\pi\hbar^2 a_s/m$ is the 3D two-body interaction strength, determined via the s -wave scattering length a_s ⁵³. As shown in the Appendix, fixing the radial component of the BEC wave function to this Thomas-Fermi ground state gives the 1D GPE Eq. (9) with effective 1D parameters

$$g_{1D} = \frac{4g_{3D}}{3\pi R_{\perp}^2} \quad (10)$$

$$K_{1D} = \frac{2K_{3D}}{\pi^2 R_{\perp}^4} \quad (11)$$

We set the 3D three body recombination loss rate coefficient to $K_{3D} = 4 \times 10^{-41} \text{ m}^6/\text{s}$, which is the value determined from our previous experiments with ⁸⁵Rb BEC³⁵. All our simulations of Eq. 9 were performed using split-step Fourier and fourth-order Runge-Kutta methods.

We consider a BEC of $N = 10^5$ ⁸⁵Rb atoms with an initial scattering length of $5a_0$ (where a_0 is the Bohr radius), prepared in a cylindrically-symmetric harmonic trap with radial and axial frequencies $\omega_{\perp} = 2\pi \times 70$ Hz and $\omega_z = 2\pi \times 10$ Hz, respectively. These are typical parameters for previous experiments^{35,54}, and give a fixed radial Thomas-Fermi radius of $R_{\perp} = 2.77 \mu\text{m}$.

The initial wave function for the simulations is a Gaussian,

$$\psi_0(z) = \frac{\sqrt{N}}{(\pi\sigma_c^2)^{1/4}} e^{-(z-z_0)^2/(2\sigma_c^2)} e^{ikz}, \quad (12)$$

where z_0 is the initial position of the atomic cloud, $\sigma_c/\sqrt{2}$ is the standard deviation of the density profile, corresponding to a k -space density standard deviation of $1/(\sqrt{2}\sigma_c)$ (full width at half maximum (FWHM) of $\Delta k = 2\sqrt{\ln 2}/\sigma_c$), and $\hbar k$ is the condensate's initial momentum. A Gaussian wave packet of this functional form could be engineered experimentally by delta-kick cooling^{36,40,41} the cloud after turning off the axial confinement, and then imparting a momentum kick $\hbar k$ to the atoms via a shallow angle Bragg transition^{28,44,45}.

Immediately before evolution, the scattering length is quenched from $5a_0$ to values $-1a_0$, 0 or $+1a_0$. This can be experimentally achieved using a Feshbach resonance^{35,55,56}. The laser barriers are also turned on at this point; these are modelled as two Gaussian potentials separated by a distance d (cavity length):

$$V(z) = V_0 \left[e^{-(z-z_{01})^2/(2\sigma_b^2)} + e^{-(z-z_{02})^2/(2\sigma_b^2)} \right], \quad (13)$$

where σ_b is the standard deviation of each barrier and z_{01} and z_{02} are the position of first and second barriers, respectively. We choose $z_{01} = z_0 + 3(\sigma_c + \sigma_b) + 15l_z$ and $z_{02} = z_{01} + 3\sigma_b + d + 3\sigma_b$ so that introducing the barrier potentials does not perturb the initial atomic cloud. Here $l_z = \sqrt{\hbar/m\omega_z}$ is the harmonic oscillator length scale of the axial trap that the BEC is initially condensed into.

Our simulations allow us to determine the number of atoms transmitted (N_T) and reflected (N_R) through the double barrier system. We investigate the resonant transmission by computing the total transmission coefficient

$$T = \frac{N_T}{N_T + N_R}, \quad (14)$$

at the time when there are no atoms left in the cavity (i.e. $N - N_T - N_R < 1$) and both N_T and N_R have reached a constant value (more precisely, do not change by more than 0.1 in a given time step).

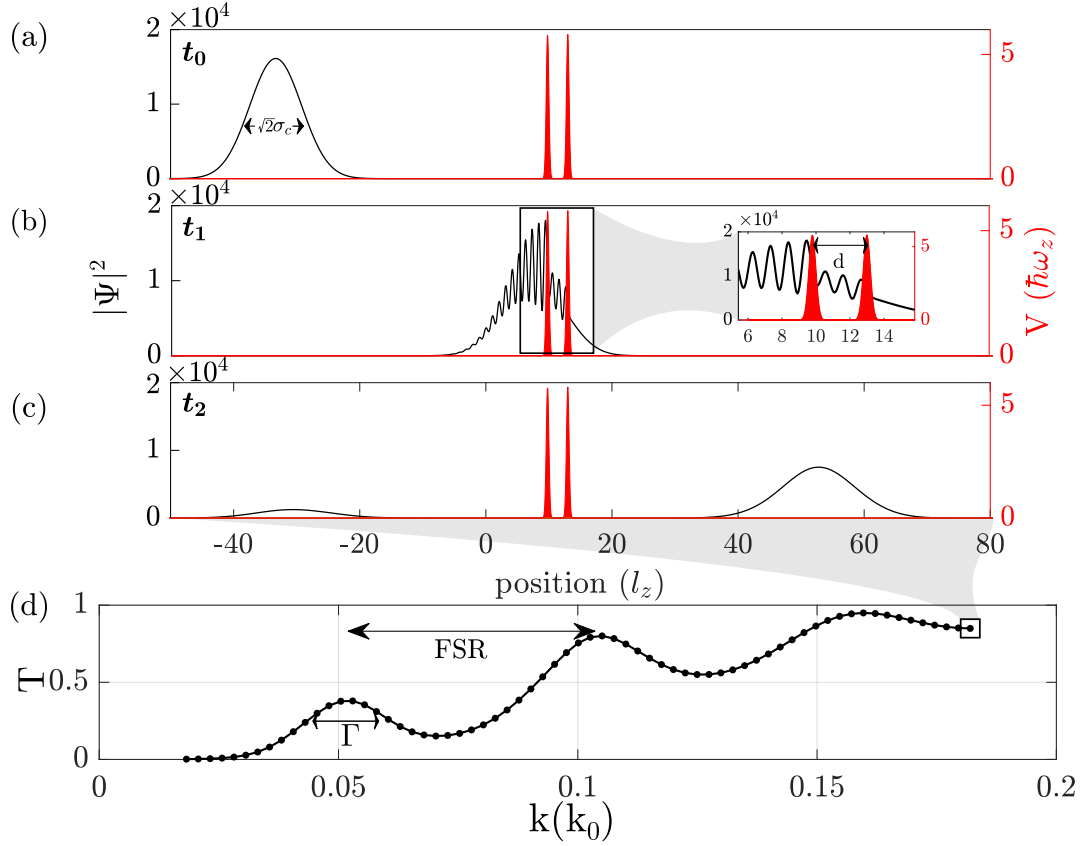


Figure 4. (a), (b) and (c) show the propagation of a non-interacting BEC having mean momentum $\hbar k = 0.182\hbar k_0$ and FWHM momentum width $\hbar\Delta k = 0.017\hbar k_0$ through two Gaussian barriers, in three snapshots in time, simulated using the 1D GPE Eq. (9). The red curves indicate the Gaussian barriers and the black curves represent the density profile of the Gaussian cloud. The BEC starts on the left side of the barriers (t_0), propagates towards the barriers, and enters the cavity (t_1). The dynamics around the cavity region is expanded and illustrated in the inset plot. Some parts of the cloud are transmitted through the barriers, whereas other parts are reflected, depending on the momentum of the cloud (t_2). (d) The transmission coefficient as a function of the momentum centre of the wave packet [here $k_0 = 2\pi/(780\text{nm})$].

Analysis of resonant transmission

Using the parameters determined above, we first simulate the resonant transmission of a non-interacting BEC passing through the double Gaussian barrier system described previously. We choose a cloud having momentum width close to the smallest experimentally-realised value of $\Delta k = 0.02k_0$ ³⁶ which in turn fixes the spatial width of the cloud to $\sigma_c \approx 12\mu\text{m}$. The propagation of this BEC at $a_s = 0$ and momentum kick $\hbar k = 0.182\hbar k_0$ is schematically shown in Fig. 4(a), (b) and (c), where (a), (b) and (c) correspond to three snapshots in time: prior to interaction, during interaction, and after interaction with the barrier, respectively. The interference caused from the overlapping incident and reflected cloud components is clearly seen in Fig. 4(b). As expected, this behaviour is present both after the initial reflection, outside of the cavity, and through multiple reflections inside the cavity. Resonant transmission is observed for the k values which are resonant with the cavity. The transmission coefficient as a function of momentum kick given to the cloud is plotted in Fig. 4(d). This confirms that Fabry-Perot resonances can indeed be observed for our parameter choice.

Instead of the maximum height expected for Fabry-Perot resonances in the case of a incident plane wave source^{37,57}, the transmission peaks observed here are suppressed, i.e. $T_{\text{max}} < 1$, reducing the contrast of the resonance peaks. A previous theoretical investigation observed this behaviour for the resonance of a non-interacting CW atom laser beam²³. The reduction in resonant transmission arises due to the finite momentum width of the source BEC. This also causes broadening of the peaks, which reduces finesse. As the peaks are suppressed due to the momentum spread of the cloud, we expect them to improve by reducing the BEC's momentum width. To investigate this further, we study the transmission profile for a range of initial cloud momentum widths. Fig. 5 shows the height, finesse and linewidth of the first resonant peak for a non-interacting BEC with momentum width ranging from $\Delta k = 4 \times 10^{-4}k_0$ to $0.017k_0$. The resonance peaks are improved (peak height and finesse

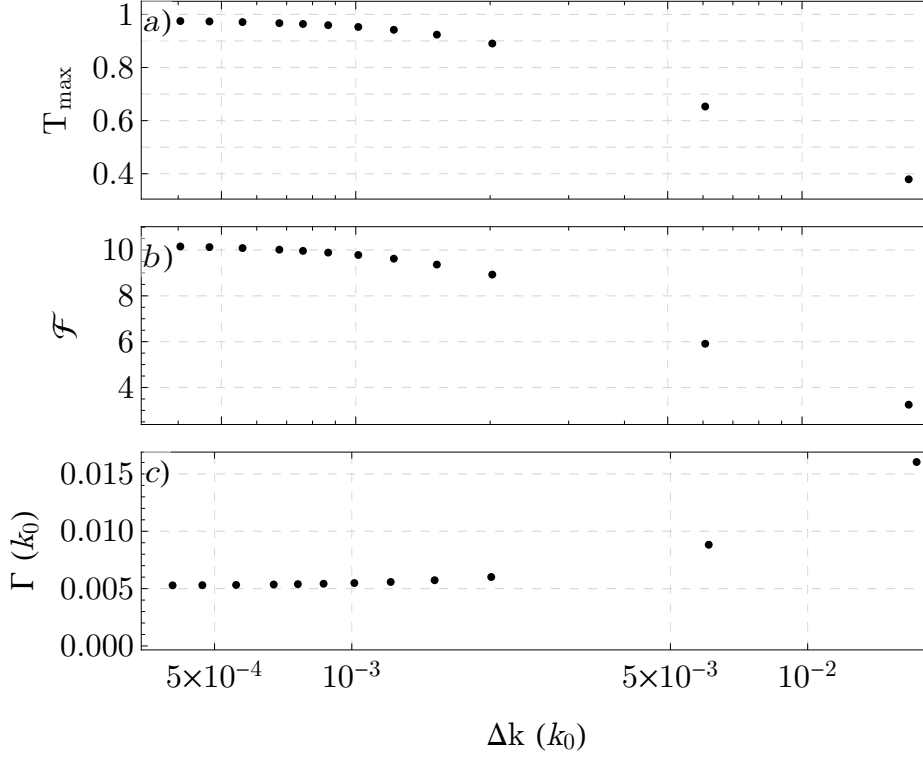


Figure 5. The influence of a non-interacting BEC’s momentum width on the (a) height, (b) finesse, and (c) linewidth of the first resonance peak. The FWHM of the initial momentum distribution, $\hbar\Delta k = 2\sqrt{\ln 2}\hbar/\sigma_c$, and linewidth are given in units of $k_0 = 2\pi/(780\text{nm})$. Peak height and finesse increase and Γ decreases with decreasing Δk .

increase and linewidth decrease) by reducing the cloud momentum width, as one would expect.

In the presence of inter-atomic interactions, the effect of three-body recombination losses become crucial. Due to the repeated reflections of the atoms between the two barriers, the density becomes very high inside the cavity, increasing the three-body recombination loss of atoms from the condensate. The overall atom loss due to three-body recombination depends non-trivially on the transmission dynamics, and so will vary with scattering length, the initial momentum kick, and spatial width of the BEC. Specifically, as the scattering length goes from positive to negative, the three-body recombination loss increases due to the difference in the propagation dynamics of the BEC as it approaches the barrier. Condensates with positive and negative scattering lengths undergo expanding or focusing, respectively, under free propagation^{48,58,59}. These dynamics modify the cloud density and therefore the overall three-body loss as well. The momentum kick imparted to the BEC further modifies the atom loss by changing the total interaction time. For larger momentum kicks, the atomic cloud propagates faster and spends less time in the high density region inside the cavity. This reduces the possibility of three-body recombination loss. Hence, as the average momentum of the cloud increases the loss rate decreases. Finally, for a fixed atom number, increasing the spatial width of the cloud (i.e. decreasing the momentum width) decreases the overall 3-body loss due to the reduction in initial density.

The transmission resonances corresponding to clouds having $a_s = -1a_0$ and $+1a_0$ and a momentum width $\Delta k = 0.017k_0$ are illustrated by the blue dashed curves in Fig. 6(a) and (b), respectively. In the presence of inter-atomic interactions the peaks are either further suppressed or not well-defined, as compared to the non-interacting cloud. This reduction in contrast is caused by the additional interaction-induced expansion of the BEC’s momentum distribution, scattering-length-dependent distortions in the momentum distribution that occur during interaction with barriers⁴⁸, and non-trivial intra-cavity dynamics due to the presence of inter-atomic interactions.

In order to mitigate the loss of contrast caused by inter-atomic interactions, we can either decrease the interactions or reduce the initial momentum width. Both approaches effectively reduce the initial interaction energy of the cloud. Figure 6 shows the effects of two methods to reduce interactions, firstly by reducing atom number and secondly by reducing the magnitude of the scattering length. Figure 6(a) and (b) show the resonance peaks for $a_s = -1a_0$ and $+1a_0$, respectively, for atom numbers $N = 10^5, 10^4$ and 10^3 . Resonance peak contrast increases substantially by reducing atom number for both attractive and repulsive clouds. For comparison, Fig. 6(c) and (d) illustrates the effect of reducing the magnitude of the scattering length

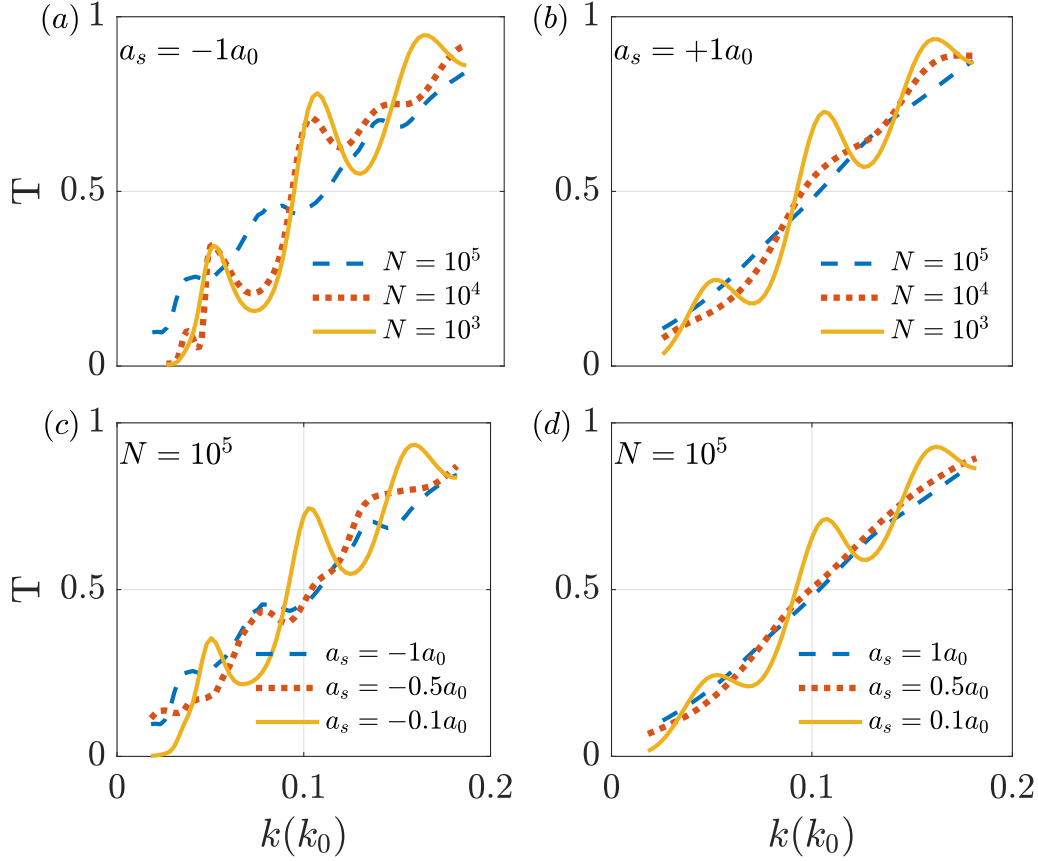


Figure 6. Shows that reducing interatomic interactions improves the resonant transmission peaks. Interaction is reduced by reducing density (by reducing atom number) in plots (a) & (b) for $a_s = -1a_0$ and $a_s = +1a_0$ respectively. In plots (c) & (d), the interaction is reduced by reducing magnitude of negative and positive scattering lengths respectively for BECs with atom number $N = 10^5$.

on the resonance peaks for attractive and repulsive clouds, respectively. Similar to the effect seen from the reduction in atom number, reducing the magnitude of the scattering length also improves the resonant peaks for both attractive and repulsive clouds.

Although reducing the initial momentum width pushes the cloud outside of the current experimentally-realizable regime, it is important to understand the system dynamics in this narrow momentum width regime. The effect of reducing momentum width on the Fabry-Perot transmission spectrum for clouds having scattering length $a_s = -1a_0$ and $+1a_0$ are shown in Fig. 7 (a) and (b), respectively. Figure 7(c) is produced by selecting the maximum transmission of the middle resonance. Here, the general trend towards $T_{\max} = 1$ is evident as the momentum width of the cloud approaches 0.

This numerical analysis shows that an atomic Fabry-Perot interferometer with a pulsed BEC source can be experimentally achieved using current technology. Since the inter-atomic interactions reduce the resonant transmission, it is ideal to use a non-interacting cloud or a weakly-interacting cloud with small to moderate atom numbers. Additionally, as current cooling techniques improve, allowing narrower momentum width sources, it may be possible to operate a ‘good’ quality atomic Fabry-Perot interferometer with a strongly-interacting cloud.

Conclusion

We have compared the properties of optical and atomic Fabry-Perot interferometers. By analysing the dependence of finesse and transmission coefficient on barrier height, barrier width, cavity length, incident atomic energy and cloud momentum width, we have determined an experimentally feasible parameter regime for observing atomic Fabry-Perot resonances. Using these parameters, we numerically simulated the transmission dynamics of a ^{85}Rb BEC through two Gaussian barriers. The simulations showed that the Fabry-Perot resonances can be achieved for a non-interacting BEC with a momentum width around

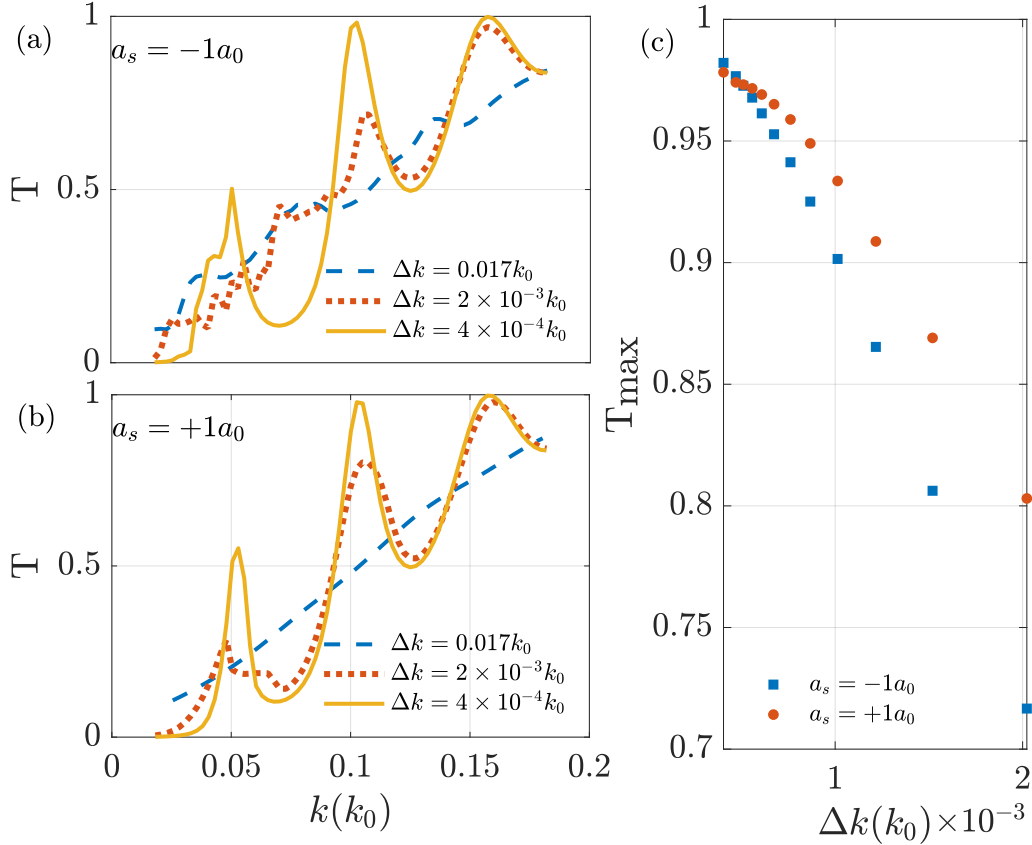


Figure 7. Illustrates that reducing initial momentum width of the cloud improves the transmission resonance peaks. (a) and (b) show the resonant peaks for $a_s = -1a_0$ and $+1a_0$ respectively, for three values of cloud momentum widths. (c) plots the height of the second peak in the resonant spectrum (T_{\max}) as a function of momentum width of the cloud, for scattering lengths $a_s = -1a_0$ and $+1a_0$. It shows that peak height increases with decreasing momentum width.

$0.02\hbar k_0$. Due to the finite momentum width of BEC, the transmission peaks are suppressed ($T_{\max} < 1$) leading to wider peaks and reduced finesse. Consequently, reducing momentum width can increase finesse and improve resonance peaks in the atomic Fabry-Perot spectrum. The introduction of inter-atomic interactions further modify and suppress the resonance peaks. We have investigated different possibilities for improving the quality of the resonant peaks of an interacting BEC, which includes reducing the interactions (by reducing atom number and/or the magnitude of the scattering length) and reducing the initial momentum width of the BEC. We have shown that both methods can improve the quality of resonances and we have illustrated that almost complete transmission ($T_{\max} \approx 1$) is achievable even for BECs having attractive and repulsive interactions. Our investigation shows that Fabry-Perot resonances can be observed only for atomic species with very low interactions or with tunable interactions, such as ^{85}Rb . This study paves the way to experimentally realise an atomic Fabry-Perot interferometer using an interacting and non-interacting pulsed BEC, that could potentially be used for many applications including velocity filtering, accelerometry and for identifying bosonic and fermionic isotopes of an element.

References

1. Gallatin, G. M. & Gould, P. L. Laser focusing of atomic beams. *JOSA B* **8**, 502–508, DOI: [10.1364/JOSAB.8.000502](https://doi.org/10.1364/JOSAB.8.000502) (1991).
2. Balykin, V. I., Letokhov, V. S., Ovchinnikov, Y. B. & Sidorov, A. I. Reflection of an atomic beam from a gradient of an optical field. *JETP Letters* **45**, 353–356 (1987).
3. Moskowitz, P. E., Gould, P. L., Atlas, S. R. & Pritchard, D. E. Diffraction of an Atomic Beam by Standing-Wave Radiation. *Physical Review Letters* **51**, 370–373, DOI: [10.1103/PhysRevLett.51.370](https://doi.org/10.1103/PhysRevLett.51.370) (1983).
4. Becker, U. Molecular physics: Matter-wave interference made clear. *Nature* **474**, 586–587, DOI: [10.1038/474586a](https://doi.org/10.1038/474586a) (2011).

5. Bongs, K. *et al.* Waveguide for Bose-Einstein condensates. *Physical Review A* **63**, 031602, DOI: [10.1103/PhysRevA.63.031602](https://doi.org/10.1103/PhysRevA.63.031602) (2001).
6. Mewes, M.-O. *et al.* Output Coupler for Bose-Einstein Condensed Atoms. *Physical Review Letters* **78**, 582–585, DOI: [10.1103/PhysRevLett.78.582](https://doi.org/10.1103/PhysRevLett.78.582) (1997).
7. Robins, N. P., Figl, C., Jeppesen, M., Dennis, G. R. & Close, J. D. A pumped atom laser. *Nature Physics* **4**, 731–736, DOI: [10.1038/nphys1027](https://doi.org/10.1038/nphys1027) (2008).
8. Contributors. In Berman, P. R. (ed.) *Atom Interferometry*, ix–xi, DOI: [10.1016/B978-012092460-8/50000-X](https://doi.org/10.1016/B978-012092460-8/50000-X) (Academic Press, San Diego, 1997).
9. Keith, D. W., Ekstrom, C. R., Turchette, Q. A. & Pritchard, D. E. An interferometer for atoms. *Physical Review Letters* **66**, 2693–2696, DOI: [10.1103/PhysRevLett.66.2693](https://doi.org/10.1103/PhysRevLett.66.2693) (1991).
10. Bouchendir, R., Cladé, P., Guellati-Khélifa, S., Nez, F. m. c. & Biraben, F. m. c. New determination of the fine structure constant and test of the quantum electrodynamics. *Phys. Rev. Lett.* **106**, 080801, DOI: [10.1103/PhysRevLett.106.080801](https://doi.org/10.1103/PhysRevLett.106.080801) (2011).
11. Parker, R. H., Yu, C., Zhong, W., Estey, B. & Müller, H. Measurement of the fine-structure constant as a test of the Standard Model. *Science* **360**, 191–195, DOI: [10.1126/science.aap7706](https://doi.org/10.1126/science.aap7706) (2018).
12. Peters, A., Chung, K. Y. & Chu, S. High-precision gravity measurements using atom interferometry. *Metrologia* **38**, 25 (2001).
13. Altin, P. A. *et al.* Precision atomic gravimeter based on Bragg diffraction. *New Journal Physics* **15**, 023009, DOI: [10.1088/1367-2630/15/2/023009](https://doi.org/10.1088/1367-2630/15/2/023009) (2013).
14. Freier, C. *et al.* Mobile quantum gravity sensor with unprecedented stability. *Journal Physics: Conference Series* **723**, 012050, DOI: [10.1088/1742-6596/723/1/012050](https://doi.org/10.1088/1742-6596/723/1/012050) (2016).
15. Stockton, J. K., Takase, K. & Kasevich, M. A. Absolute Geodetic Rotation Measurement Using Atom Interferometry. *Physical Review Letters* **107**, 133001, DOI: [10.1103/PhysRevLett.107.133001](https://doi.org/10.1103/PhysRevLett.107.133001) (2011).
16. Savoie, D. *et al.* Interleaved atom interferometry for high-sensitivity inertial measurements. *Science Advances* **4** (2018).
17. Xue, J. *et al.* Pulsed laser linewidth measurement using Fabry–Pérot scanning interferometer. *Results Physics* **6**, 698–703, DOI: [10.1016/j.rinp.2016.10.004](https://doi.org/10.1016/j.rinp.2016.10.004) (2016).
18. Drever, R. W. P. *et al.* Laser phase and frequency stabilization using an optical resonator. *Applied Physics B* **31**, 97–105, DOI: [10.1007/BF00702605](https://doi.org/10.1007/BF00702605) (1983).
19. Taylor, H. F. Principles and applications of fiber-optic Fabry-Perot sensors. In *Technical Digest. Summaries of Papers Presented at the Conference on Lasers and Electro-Optics. Conference Edition. 1998 Technical Digest Series, Vol.6 (IEEE Cat. No.98CH36178)*, 312–, DOI: [10.1109/CLEO.1998.676211](https://doi.org/10.1109/CLEO.1998.676211) (1998).
20. Islam, M. R., Ali, M. M., Lai, M.-H., Lim, K.-S. & Ahmad, H. Chronology of Fabry-Perot Interferometer Fiber-Optic Sensors and Their Applications: A Review. *Sensors* **14**, 7451–7488, DOI: [10.3390/s140407451](https://doi.org/10.3390/s140407451) (2014).
21. Dutt, A. & Kar, S. Smooth double barriers in quantum mechanics. *American Journal Physics* **78**, 1352–1360, DOI: [10.1119/1.3481701](https://doi.org/10.1119/1.3481701) (2010).
22. Ruschhaupt, A., Delgado, F. & Muga, J. G. Velocity selection of ultra-cold atoms with Fabry–Perot laser devices: improvements and limits. *Journal Physics B: At. Molecular Optical Physics* **38**, 2665–2674, DOI: [10.1088/0953-4075/38/15/007](https://doi.org/10.1088/0953-4075/38/15/007) (2005).
23. Damon, F., Vermersch, F., Muga, J. G. & Guéry-Odelin, D. Reduction of local velocity spreads by linear potentials. *Physical Review A* **89**, 053626, DOI: [10.1103/PhysRevA.89.053626](https://doi.org/10.1103/PhysRevA.89.053626) (2014).
24. Lee, S. K., Lee, H. S., Kim, J. M. & Cho, D. Optical dipole trap using a Fabry–Perot interferometer as a power buildup cavity. *Journal Physics B: At. Molecular Optical Physics* **38**, 1381–1389, DOI: [10.1088/0953-4075/38/8/023](https://doi.org/10.1088/0953-4075/38/8/023) (2005).
25. Wilkens, M., Goldstein, E., Taylor, B. & Meystre, P. Fabry-Pérot interferometer for atoms. *Physical Review A* **47**, 2366–2369, DOI: [10.1103/PhysRevA.47.2366](https://doi.org/10.1103/PhysRevA.47.2366) (1993).
26. Debs, J. E. *et al.* Cold-atom gravimetry with a Bose-Einstein condensate. *Phys. Rev. A* **84**, 033610 (2011).
27. Szigeti, S. S., Debs, J. E., Hope, J. J., Robins, N. P. & Close, J. D. Why momentum width matters for atom interferometry with bragg pulses. *New Journal Physics* **14**, 023009 (2012).

28. Hardman, K. *et al.* Simultaneous Precision Gravimetry and Magnetic Gradiometry with a Bose-Einstein Condensate: A High Precision, Quantum Sensor. *Physical Review Letters* **117**, 138501, DOI: [10.1103/PhysRevLett.117.138501](https://doi.org/10.1103/PhysRevLett.117.138501) (2016).
29. Rapedius, K. & Korsch, H. J. Barrier transmission for the one-dimensional nonlinear Schrödinger equation: Resonances and transmission profiles. *Physical Review A* **77**, 063610, DOI: [10.1103/PhysRevA.77.063610](https://doi.org/10.1103/PhysRevA.77.063610) (2008).
30. Carusotto, I. Nonlinear atomic Fabry-Perot interferometer: From the mean-field theory to the atom blockade effect. *Physical Review A* **63**, 023610, DOI: [10.1103/PhysRevA.63.023610](https://doi.org/10.1103/PhysRevA.63.023610) (2001).
31. Paul, T., Richter, K. & Schlagheck, P. Nonlinear Resonant Transport of Bose-Einstein Condensates. *Physical Review Letters* **94**, 020404, DOI: [10.1103/PhysRevLett.94.020404](https://doi.org/10.1103/PhysRevLett.94.020404) (2005).
32. Paul, T., Hartung, M., Richter, K. & Schlagheck, P. Nonlinear transport of Bose-Einstein condensates through mesoscopic waveguides. *Physical Review A* **76**, 063605, DOI: [10.1103/PhysRevA.76.063605](https://doi.org/10.1103/PhysRevA.76.063605) (2007).
33. Ernst, T., Paul, T. & Schlagheck, P. Transport of ultracold Bose gases beyond the Gross-Pitaevskii description. *Physical Review A* **81**, 013631, DOI: [10.1103/PhysRevA.81.013631](https://doi.org/10.1103/PhysRevA.81.013631) (2010).
34. Robins, N. P., Altin, P. A., Debs, J. E. & Close, J. D. Atom lasers: Production, properties and prospects for precision inertial measurement. *Physics Reports* **529**, 265–296 (2013).
35. Everitt, P. J. *et al.* Observation of a modulational instability in Bose-Einstein condensates. *Phys. Rev. A* **96**, 041601, DOI: [10.1103/PhysRevA.96.041601](https://doi.org/10.1103/PhysRevA.96.041601) (2017).
36. Kovachy, T. *et al.* Matter Wave Lensing to Picokelvin Temperatures. *Physical Review Letters* **114**, 143004, DOI: [10.1103/PhysRevLett.114.143004](https://doi.org/10.1103/PhysRevLett.114.143004) (2015).
37. Xiao, Z., Huang, H. & Lu, X.-X. Resonant tunneling dynamics and the related tunneling time. *International Journal Modern Physics B* **29**, 1550052, DOI: [10.1142/S0217979215500526](https://doi.org/10.1142/S0217979215500526) (2015).
38. Roberts, J. L. *et al.* Resonant Magnetic Field Control of Elastic Scattering in Cold R85b. *Physical Review Letters* **81**, 5109–5112, DOI: [10.1103/PhysRevLett.81.5109](https://doi.org/10.1103/PhysRevLett.81.5109) (1998).
39. Kuhn, C. C. N. *et al.* A Bose-condensed, simultaneous dual-species Mach-Zehnder atom interferometer. *New Journal Physics* **16**, 073035, DOI: [10.1088/1367-2630/16/7/073035](https://doi.org/10.1088/1367-2630/16/7/073035) (2014).
40. Ammann, H. & Christensen, N. Delta Kick Cooling: A New Method for Cooling Atoms. *Physical Review Letters* **78**, 2088–2091, DOI: [10.1103/PhysRevLett.78.2088](https://doi.org/10.1103/PhysRevLett.78.2088) (1997).
41. McDonald, G. D. *et al.* $\hbar k$ momentum separation with Bloch oscillations in an optically guided atom interferometer. *Physical Review A* **88**, 053620, DOI: [10.1103/PhysRevA.88.053620](https://doi.org/10.1103/PhysRevA.88.053620) (2013).
42. Vaughan, J. M. *The Fabry-Perot Interferometer History, Theory, Practice and Applications*. Series on Optics and Optoelectronics (Taylor & Francis, 1989).
43. Adam Steck, D. Rubidium 85 D Line Data (2013).
44. Stenger, J. *et al.* Bragg Spectroscopy of a Bose-Einstein Condensate. *Physical Review Letters* **82**, 4569–4573, DOI: [10.1103/PhysRevLett.82.4569](https://doi.org/10.1103/PhysRevLett.82.4569) (1999).
45. Ernst, P. T. *et al.* Probing superfluids in optical lattices by momentum-resolved Bragg spectroscopy. *Nature Physics* **6**, 56–61, DOI: [10.1038/nphys1476](https://doi.org/10.1038/nphys1476) (2010).
46. Salasnich, L., Parola, A. & Reatto, L. Pulsed macroscopic quantum tunneling of falling bose-einstein condensates. *Phys. Rev. A* **64**, 023601, DOI: [10.1103/PhysRevA.64.023601](https://doi.org/10.1103/PhysRevA.64.023601) (2001).
47. Carr, L. D., Holland, M. J. & Malomed, B. A. Macroscopic quantum tunnelling of bose-einstein condensates in a finite potential well. *Journal Physics B: At. Molecular Optical Physics* **38**, 3217–3231, DOI: [10.1088/0953-4075/38/17/012](https://doi.org/10.1088/0953-4075/38/17/012) (2005).
48. Manju, P. *et al.* Quantum tunneling dynamics of an interacting Bose-Einstein condensate through a Gaussian barrier. *Physical Review A* **98**, 053629, DOI: [10.1103/PhysRevA.98.053629](https://doi.org/10.1103/PhysRevA.98.053629) (2018).
49. Oliver J. Wales, T. P. B. J. L. H. S. A. G. S. L. C., Ana Rakonjac. Splitting and recombination of bright-solitary-matter waves. *arXiv:1906.06083* (2019).
50. Altin, P. A. *et al.* Collapse and three-body loss in a ^{85}Rb Bose-Einstein condensate. *Physical Review A* **84**, 033632, DOI: [10.1103/PhysRevA.84.033632](https://doi.org/10.1103/PhysRevA.84.033632) (2011).
51. Salasnich, L., Parola, A. & Reatto, L. Effective wave equations for the dynamics of cigar-shaped and disk-shaped bose condensates. *Phys. Rev. A* **65**, 043614 (2002).

52. Wigley, P. B. *et al.* Precise wave-function engineering with magnetic resonance. *Phys. Rev. A* **96**, 013612 (2017).
53. Dalfovo, F., Giorgini, S., Pitaevskii, L. P. & Stringari, S. Theory of bose-einstein condensation in trapped gases. *Rev. Mod. Phys.* **71**, 463–512 (1999).
54. Wigley, P. B. *et al.* Non-destructive shadowgraph imaging of ultra-cold atoms. *Optics Letters* **41**, 4795–4798, DOI: [10.1364/OL.41.004795](https://doi.org/10.1364/OL.41.004795) (2016).
55. McDonald, G. D. *et al.* Bright Solitonic Matter-Wave Interferometer. *Phys. Rev. Lett.* **113**, 013002, DOI: [10.1103/PhysRevLett.113.013002](https://doi.org/10.1103/PhysRevLett.113.013002) (2014).
56. McDonald, G. D. *et al.* Erratum: Bright Solitonic Matter-Wave Interferometer [Phys. Rev. Lett. 113, 013002 (2014)]. *Phys. Rev. Lett.* **118**, 219903, DOI: [10.1103/PhysRevLett.118.219903](https://doi.org/10.1103/PhysRevLett.118.219903) (2017).
57. Uma Maheswari, A., Prema, P., Mahadevan, S. & Shastry, C. S. Quasi-bound states, resonance tunnelling, and tunnelling times generated by twin symmetric barriers. *Pramana* **73**, 969, DOI: [10.1007/s12043-009-0173-x](https://doi.org/10.1007/s12043-009-0173-x) (2009).
58. Dekel, G., Farberovich, O. V., Soffer, A. & Fleurov, V. Nonlinear dynamic phenomena in macroscopic tunneling. *Physica D: Nonlinear Phenomena* **238**, 1475–1481, DOI: [10.1016/j.physd.2008.06.013](https://doi.org/10.1016/j.physd.2008.06.013) (2009).
59. Carr, L. D., Holland, M. J. & Malomed, B. A. Macroscopic quantum tunnelling of Bose–Einstein condensates in a finite potential well. *Journal Physics B: At. Molecular Optical Physics* **38**, 3217–3231, DOI: [10.1088/0953-4075/38/17/012](https://doi.org/10.1088/0953-4075/38/17/012) (2005).

Acknowledgements

We acknowledge useful discussions with S.A. Haine and A.C. White. This research was supported by funding from the Australian Research Council Project No. DP160104965 and was undertaken with the assistance of resources and services from the National Computational Infrastructure (NCI), which is supported by the Australian Government.

Author contributions statement

The theoretical analysis and numerical simulations were carried out by PM under the supervision of KSH, PBW, and SSS. JDC and all other authors contributed to the interpretation of results and the writing of the manuscript.

Additional information

Competing interests: The authors declare no competing interests.

Appendix: Dimensional Reduction of 3D GPE to 1D GPE

Consider the 3D GPE describing the macroscopic wave function of a BEC:

$$i\hbar \frac{\partial \Psi(\mathbf{r}, t)}{\partial t} = \left[-\frac{\hbar^2}{2m} \nabla^2 + V_{\text{ext}}(\mathbf{r}, t) + g_{3\text{D}} |\Psi(\mathbf{r}, t)|^2 - i\hbar K_{3\text{D}} |\Psi(\mathbf{r}, t)|^4 \right] \Psi(\mathbf{r}, t) \quad (15)$$

where V_{ext} is an external trapping potential of the form

$$V_{\text{ext}}(\mathbf{r}, t) = \frac{1}{2} m \omega_{\perp}^2 (x^2 + y^2) + V(z, t) \equiv V_{\perp}(x, y) + V(z, t). \quad (16)$$

Here m is the atomic mass and ω_{\perp} is the frequency of the radial harmonic trap. For a sufficiently tight radial confinement (large ω_{\perp}), the wave function dynamics are approximately independent of the radial degrees of freedom. This therefore allows us to assume a separable BEC wave function of the form

$$\Psi(\mathbf{r}, t) = \phi(x, y) \psi(z, t), \quad (17)$$

where $\phi(x, y)$ is normalised to unity and $\psi(z, t)$ is normalised to the atom number, $N(t)$ (atom number can vary with time due to three-body recombination losses). Multiplying Eq. (15) by $\phi^*(x, y)$ and integrating over x and y gives,

$$i\hbar \frac{\partial \psi(z, t)}{\partial t} = \left[-\frac{\hbar^2}{2m} \frac{\partial^2}{\partial z^2} + V(z, t) + g_{3\text{D}} \left(\int dx dy |\phi(x, y)|^4 \right) |\psi(z, t)|^2 - i\hbar K_{3\text{D}} \left(\int dx dy |\phi(x, y)|^6 \right) |\psi(z, t)|^4 \right. \\ \left. \left(-\frac{\hbar^2}{2m} \int dx dy \phi^*(x, y) \left(\frac{\partial^2}{\partial x^2} + \frac{\partial^2}{\partial y^2} \right) \phi(x, y) \right) + \left(\int dx dy \phi^*(x, y) V_{\perp}(x, y) \phi(x, y) \right) \right] \psi(z, t). \quad (18)$$

We assume that the BEC is initially condensed into a cylindrically-symmetric harmonic trap with radial and axial trapping frequencies ω_{\perp} and ω_z , respectively. We further assume that this initially-prepared condensate has strong inter-atomic interactions, and is therefore within the Thomas-Fermi regime. In this case, $\phi(x, y)$ corresponds to the Thomas-Fermi ground state

$$\phi(x, y) = \max \left\{ 0, \sqrt{\frac{2}{\pi R_{\perp}^2}} \left(1 - \frac{x^2}{R_{\perp}^2} - \frac{y^2}{R_{\perp}^2} \right) \right\}, \quad (19)$$

with chemical potential and Thomas-Fermi radius

$$\mu_{3D} = \left[\frac{15N g_{3D} \omega_{\perp}^2 \omega_z}{8\pi} \left(\frac{m}{2} \right)^{3/2} \right]^{2/5}, \quad (20)$$

$$R_{\perp} = \sqrt{\frac{2\mu_{3D}}{m\omega_{\perp}^2}}, \quad (21)$$

respectively. The Thomas-Fermi approximation allows us to neglect the kinetic energy term in the second line of Eq. (18). Furthermore, the integral over $V_{\perp}(x, y)$ results in a constant energy shift, which can be neglected. Finally, noting that

$$\int dx dy |\phi(x, y)|^4 = \frac{4}{3\pi R_{\perp}^2}, \quad (22)$$

$$\int dx dy |\phi(x, y)|^6 = \frac{2}{\pi^2 R_{\perp}^4}, \quad (23)$$

yields the effective 1D GPE Eq. (9) with g_{1D} and K_{1D} given by Eq. (10) and Eq. (11), respectively.